

Vortices in a mesoscopic superconducting circular sector

Edson Sardella, Paulo Noronha Lisboa-Filho, and André Luiz Malvezzi

*Departamento de Física, Faculdade de Ciências
Universidade Estadual Paulista-UNESP*

Caixa Postal 473, 17033-360, Bauru-SP, Brazil

(Dated: October 21, 2021)

In the present paper we develop an algorithm to solve the time dependent Ginzburg-Landau (TDGL) equations, by using the link variables technique, for circular geometries. In addition, we evaluate the Helmholtz and Gibbs free energy, the magnetization, and the number of vortices. This algorithm is applied to a circular sector. We evaluate the superconducting-normal magnetic field transition, the magnetization, and the superconducting density. Furthermore, we study the nucleation of giant and multi-vortex states for that geometry.

I. INTRODUCTION

The advances in the technologies of nanofabrication in the last few decades allowed intensive investigation efforts in nanostructured superconductors, both in the experimental and theoretical fronts. It is well known that, for very confined geometries, the superconducting-normal (SN) magnetic field transition is increased extraordinarily. It was experimentally observed that for an Al square very thin film with a size of few micrometers the upper critical field $H_{c2}(T)$ can be increased up to 3.32 with the inclusion of defects, 2.01 larger than the usual value of $H_{c2}(T)$.^{1,2} Furthermore, numerical simulations carried out in a circular wedge (see Ref. 3 and references therein), have shown that, by keeping the area of this geometry constant, the SN transition field is a uniform increasing function with decreasing the angular width Θ and diverges as the angle goes to zero.

Another important issue in confined geometries is the occurrence of giant vortices. The experimental observation of giant vortex in mesoscopic superconductor is still a controversial issue. Through multi-small-tunnel-junction measurements in an Al thin disk film, Kanda *et al.*⁴ have argued that, as the vorticity increases, giant vortex configuration will occur. On the other hand, scanning SQUID microscopy on Nb thin film, both square and triangle, cannot guarantee giant vortex configurations, at least for low vorticity.^{5,6} Early numerical simulation of the present authors⁷ have shown the dynamic of the nucleation of giant and multi-vortex state before they set into an equilibrium configuration for a square geometry.

It is well known that the phenomenology of superconductivity can be described by the time dependent Ginzburg-Landau (TDGL) equations.⁹ The present contribution uses the TDGL approach to address the issues above, namely, of the nucleation of vortices in confined geometries and the behavior of the transition field for a deformable geometry. For this, we have chosen a circular sector (see Fig. 1), where we can arbitrarily change its shape. To our best knowledge, the discretization of the TDGL equations, by using the link variables technique, has been done only in rectangular coordinates.^{10,11} So, we will extend this algorithm to circular geometries by

using polar coordinates. Our procedure makes possible to generalize the algorithm to any geometry. The key point in such problem is how to write the auxiliary fields appropriately according to the system of coordinates, making the development of the present algorithm a specific algorithm necessary. Otherwise, the purpose of generalization will not be achieved. We anticipate that the two slopes of the present work will show that: (a) as we decrease the area of the circular sector, the transition field may increase for large angles, but all the curves will collapse into the asymptotic behavior $H/H_{c2}(T) = \sqrt{3}/\Theta$; and (b) only the confinement of vortices is not sufficient to obtain giant vortex state, but also the geometry is very important to favor the nucleation of such configurations. The geometry we have chosen does not allow us to assure clearly the nucleation of giant vortex. For a circular sector of several angular widths, ranging from 45° to 180° , having the same area as a disk, a square and a triangle, we did not observe the occurrence of giant vortex as previous numerical simulations have predicted for those geometries.⁸ In addition, we will show that the criterion used for nucleation of giant vortex may lead us to non conclusive pictures, at least for the geometry under the present investigation.

The paper is outlined as follows. In Section II we write the TDGL equations in a gauge invariant form by using the auxiliary field in polar coordinates. In Section III we develop the algorithm we use to solve the TDGL equations: we define the mesh used to discretize the TDGL for a circular sector, the discrete variables which are evaluated in the mesh, the boundary conditions and, finally, the important physical quantities which will be extracted from the numerical setup are determined. In Section IV we present and discuss the results of the numerical simulations for certain parameters of a superconducting circular sector.

II. THE TDGL EQUATIONS

The properties of the superconducting state are usually described by the complex order parameter ψ , for which the absolute square value $|\psi|^2$ represents the superfluid density, and the vector potential \mathbf{A} , which is related to

the local magnetic field as $\mathbf{h} = \nabla \times \mathbf{A}$. These quantities are determined by the TDGL equations, which in the non-dimensional version are given by

$$\begin{aligned} \frac{\partial \psi}{\partial t} &= -\mathbf{D} \cdot \mathbf{D} \psi + (1 - T) \psi (1 - |\psi|^2), \\ \beta \frac{\partial \mathbf{A}}{\partial t} &= (1 - T) \text{Re} [\bar{\psi} \mathbf{D} \psi] - \kappa^2 \nabla \times \mathbf{h}, \end{aligned} \quad (1)$$

where T is the temperature in units of the critical temperature; lengths are in units of $\xi(0)$, the coherence length at zero temperature, and fields in units of $H_{c2}(0)$, the upper critical field at zero temperature; β is the ratio between the relaxation times of the vector potential and the order parameter; κ is the Ginzburg-Landau parameter which is material dependent; the operator $\mathbf{D} = -i\nabla - \mathbf{A}$; Re indicates the real part of a complex variable and the overbar means the complex conjugation; (for more details, see Reference 7,10,11). Here, we will neglect the z -dependence on the order parameter. This is valid either if the system is infinite along the z -direction or if it is a very thin film of thickness $d \ll 1$. However, in the former case, κ^2 is replaced by an effective Ginzburg-Landau parameter $\kappa_{eff}^2 = \kappa^2/d$ (for instance, see References 12 and 13). The generalization to the a system of arbitrary thickness should not present any difficulty.

It is convenient to introduce the auxiliary vector field $\mathcal{U} = (\mathcal{U}_\rho, \mathcal{U}_\theta)$ in polar coordinates, which is defined by

$$\begin{aligned} \mathcal{U}_\rho(\rho, \theta) &= \exp \left(-i \int_{\rho_0}^{\rho} A_\rho(\theta, \xi) d\xi \right), \\ \mathcal{U}_\theta(\rho, \theta) &= \exp \left(-i \int_{\theta_0}^{\theta} A_\theta(\xi, \rho) \rho d\xi \right), \end{aligned} \quad (2)$$

where (ρ_0, θ_0) is an arbitrary reference point. For the sake of brevity we omit the time dependence on the fields. Notice that

$$\frac{\partial \mathcal{U}_\rho}{\partial \rho} = -i A_\rho \mathcal{U}_\rho, \quad \frac{1}{\rho} \frac{\partial \mathcal{U}_\theta}{\partial \theta} = -i A_\theta \mathcal{U}_\theta, \quad (3)$$

and that

$$D_\rho \psi = -i \bar{\mathcal{U}}_\rho \frac{\partial (\mathcal{U}_\rho \psi)}{\partial \rho}, \quad D_\theta \psi = -i \frac{\bar{\mathcal{U}}_\theta}{\rho} \frac{\partial (\mathcal{U}_\theta \psi)}{\partial \theta}. \quad (4)$$

Upon using these two last equations recursively, we obtain

$$D_\rho^2 \psi = -\bar{\mathcal{U}}_\rho \frac{\partial^2 (\mathcal{U}_\rho \psi)}{\partial \rho^2}, \quad D_\theta^2 \psi = -\frac{\bar{\mathcal{U}}_\theta}{\rho^2} \frac{\partial^2 (\mathcal{U}_\theta \psi)}{\partial \theta^2}. \quad (5)$$

As a consequence, we obtain for the kinetic term in the first TDGL equation

$$\begin{aligned} \mathbf{D} \cdot \mathbf{D} \psi &= D_\rho^2 \psi + D_\theta^2 \psi - \frac{i}{\rho} D_\rho \psi \\ &= -\frac{\bar{\mathcal{U}}_\rho}{\rho} \frac{\partial}{\partial \rho} \left[\rho \frac{\partial (\mathcal{U}_\rho \psi)}{\partial \rho} \right] - \frac{\bar{\mathcal{U}}_\theta}{\rho^2} \frac{\partial^2 (\mathcal{U}_\theta \psi)}{\partial \theta^2}. \end{aligned} \quad (6)$$

From equations (4), it can also be easily proved that

$$\begin{aligned} \text{Re}[\bar{\psi} D_\rho \psi] &= \text{Im} \left[\bar{\mathcal{U}}_\rho \bar{\psi} \frac{\partial (\mathcal{U}_\rho \psi)}{\partial \rho} \right], \\ \text{Re}[\bar{\psi} D_\theta \psi] &= \text{Im} \left[\frac{\bar{\mathcal{U}}_\theta \bar{\psi}}{\rho} \frac{\partial (\mathcal{U}_\theta \psi)}{\partial \theta} \right], \end{aligned} \quad (7)$$

where Im indicates the imaginary part of a complex variable.

Finally, by using equations (6) and (7), the TDGL equations of (1) can be rewritten as

$$\begin{aligned} \frac{\partial \psi}{\partial t} &= \frac{\bar{\mathcal{U}}_\rho}{\rho} \frac{\partial}{\partial \rho} \left[\rho \frac{\partial (\mathcal{U}_\rho \psi)}{\partial \rho} \right] + \frac{\bar{\mathcal{U}}_\theta}{\rho^2} \frac{\partial^2 (\mathcal{U}_\theta \psi)}{\partial \theta^2} \\ &\quad + (1 - T) \psi (1 - |\psi|^2), \\ \beta \frac{\partial A_\rho}{\partial t} &= (1 - T) \text{Im} \left[\bar{\mathcal{U}}_\rho \bar{\psi} \frac{\partial (\mathcal{U}_\rho \psi)}{\partial \rho} \right] - \kappa_{eff}^2 \frac{1}{\rho} \frac{\partial h_z}{\partial \theta}, \\ \beta \frac{\partial A_\theta}{\partial t} &= (1 - T) \text{Im} \left[\frac{\bar{\mathcal{U}}_\theta \bar{\psi}}{\rho} \frac{\partial (\mathcal{U}_\theta \psi)}{\partial \theta} \right] + \kappa_{eff}^2 \frac{\partial h_z}{\partial \rho}. \end{aligned} \quad (8)$$

Disregarding the non-linear term, the first TDGL equation written as above resembles a diffusion equation, except by the fact that the Laplacian appears with different weights. The weights depend locally on the components of the auxiliary field \mathcal{U} . Written like in (8), the TDGL equations are gauge invariant, that is, they do not change their form under any transformation $\psi \rightarrow \psi e^{i\chi}$, $\mathbf{A} \rightarrow \mathbf{A} + \nabla \chi$. This is a very important point for any discretization procedure of the TDGL equations. Otherwise, we may obtain non-physical numerical solutions.

III. NUMERICAL METHOD

A. The Computational Mesh

We will discretize the TDGL equations of (8) on a circular sector as illustrated in Fig. 1. The mesh consists of $N_\rho \times N_\theta$ cells with size (a_ρ, a_θ) in polar coordinates. The circular sector has internal radius r and external R ; Θ is its angular width. Let (ρ_i, θ_j) be a vertex point in the mesh, where $\rho_{i+1} = \rho_i + a_\rho$, $\theta_{j+1} = \theta_j + a_\theta$, for all $\{1 \leq i \leq N_\rho, 1 \leq j \leq N_\theta\}$; $\rho_1 = r$ and $\theta_1 = 0$; this particular choice for the initial value of the angle does not imply in lost of generality since the system is invariant under any rotation. The superconducting domain is comprehended by $\Omega_{\text{SC}} = \{\rho_1 + a_\rho/2 < \rho < \rho_{N_\rho} + a_\rho/2, a_\theta/2 < \theta < \theta_{N_\theta} + a_\theta/2\}$. The superconducting region is surrounded by a thin normal metal layer of width $a_\rho/2$ in the radial direction. Both regions are inside the domain $\Omega = \{\rho_1 < \rho < \rho_{N_\rho+1}, 0 < \theta < \theta_{N_\theta+1}\}$. We denote by $\partial\Omega_{\text{SC}}$ the interface between the superconductor and the normal metal, and by $\partial\Omega$ the normal metal-vacuum interface.

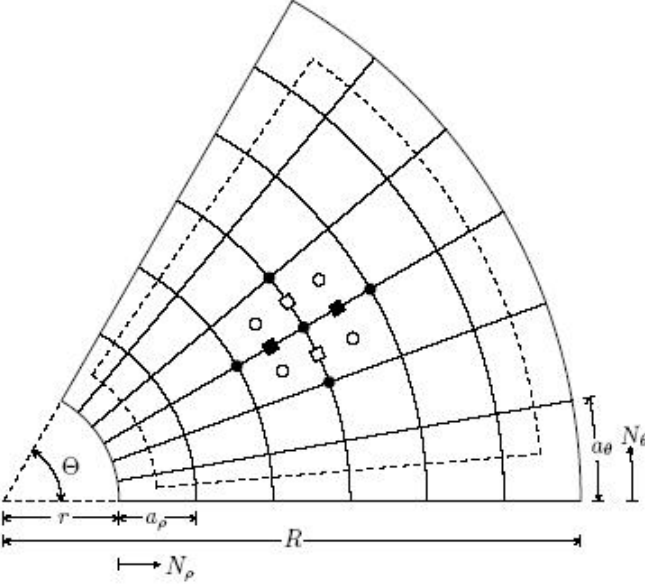


FIG. 1: The computational mesh in polar coordinates used for the evaluation of $\psi_{i,j}$ (●, vertex point); $h_{z,i,j}$ and $L_{i,j}$ (○, cell point); $A_{\rho,i,j}$ and $U_{\rho,i,j}$ (■, link point); $A_{\theta,i,j}$ and $U_{\theta,i,j}$ (□, link point). The superconducting domain is delimited by the dashed line $\partial\Omega_{SC}$, and superconductor and the normal metal are surrounded by the solid line $\partial\Omega$. Other details of the Figure are described in Section III A

B. The Discrete Variables

Let us define the following discrete variables.

- The vertex points

$$\begin{aligned}\rho_i &= r + (i-1)a_\rho, \quad 1 \leq i \leq N_\rho + 1, \\ \theta_j &= (j-1)a_\theta, \quad 1 \leq j \leq N_\theta + 1,\end{aligned}\quad (9)$$

The points $(\rho_{i+1/2} = \rho_i + a_\rho/2, \theta_{i+1/2} = \theta_i + a_\theta/2)$ are called the cell points. The points $(\rho_{i+1/2}, \theta_j)$ and $(\rho_i, \theta_{j+1/2})$ are the link points in the radial and transversal directions respectively (see Fig. 1).

- The order parameter

$$\psi_{i,j} = \psi(\rho_i, \theta_j), \quad (10)$$

for all $\{1 \leq i \leq N_\rho + 1, 1 \leq j \leq N_\theta + 1\}$.

- The vector potential

$$A_{\rho,i,j} = A_\rho(\rho_{i+1/2}, \theta_j), \quad A_{\theta,i,j} = A_\theta(\rho_i, \theta_{j+1/2}), \quad (11)$$

for all $\{1 \leq i \leq N_\rho, 1 \leq j \leq N_\theta + 1\}$, and $\{1 \leq i \leq N_\rho + 1, 1 \leq j \leq N_\theta\}$, respectively.

- The link variables

$$U_{\rho,i,j} = \bar{U}_\rho(\rho_i, \theta_j) \mathcal{U}_\rho(\rho_{i+1}, \theta_j) = \exp(-ia_\rho A_{\rho,i,j}),$$

$$U_{\theta,i,j} = \bar{U}_\theta(\rho_i, \theta_j) \mathcal{U}_\theta(\rho_i, \theta_{j+1}) = \exp(-i\rho_i a_\theta A_{\theta,i,j}), \quad (12)$$

for all $\{1 \leq i \leq N_\rho, 1 \leq j \leq N_\theta + 1\}$, and $\{1 \leq i \leq N_\rho + 1, 1 \leq j \leq N_\theta\}$, respectively.

- The local magnetic field

$$h_{z,i,j} = h_z(\rho_{i+1/2}, \theta_{j+1/2}), \quad (13)$$

for all $\{1 \leq i \leq N_\rho, 1 \leq j \leq N_\theta\}$.

In what follows, it will be important to define the following discrete variable

$$\begin{aligned}L_{i,j} &= \exp\left(-i \oint_{\partial\mathcal{D}} \mathbf{A} \cdot d\mathbf{r}\right) \\ &= \exp\left(-i \int_{\mathcal{D}} h_z \rho \, d\rho d\theta\right) \\ &= \exp(-ia_\rho \rho_{i+1/2} a_\theta h_{z,i,j}),\end{aligned}\quad (14)$$

for all $\{1 \leq i \leq N_\rho, 1 \leq j \leq N_\theta\}$, where \mathcal{D} is the domain of a unit cell limited by a closed path $\partial\mathcal{D}$. The use of the Stoke's theorem and the midpoint rule for numerical integration have been made. A simple inspection of equation (14) leads to

$$L_{i,j} = U_{\rho,i,j} U_{\theta,i+1,j} \bar{U}_{\rho,i,j+1} \bar{U}_{\theta,i,j}. \quad (15)$$

C. The Discretization of the TDGL

Now, we are in a position to discretize the TDGL equations. This can be done by using the central difference approximation for the derivatives which is second order accurate in (a_ρ, a_θ) . A tedious, however straightforward calculation, leads us to the following discrete version of the TDGL equations of (8)

$$\begin{aligned}\frac{\partial \psi_{i,j}}{\partial t} &= \mathcal{F}_{\psi,i,j}, \\ \beta \frac{\partial A_{\rho,i,j}}{\partial t} &= (1-T) \text{Im} \left[\frac{\bar{\psi}_{i,j} U_{\rho,i,j} \psi_{i+1,j}}{a_\rho} \right] \\ &\quad - \kappa_{eff}^2 \left(\frac{h_{z,i,j} - h_{z,i,j-1}}{\rho_{i+1/2} a_\theta} \right), \\ \beta \frac{\partial A_{\theta,i,j}}{\partial t} &= (1-T) \text{Im} \left[\frac{\bar{\psi}_{i,j} U_{\theta,i,j} \psi_{i,j+1}}{\rho_i a_\theta} \right] \\ &\quad + \kappa_{eff}^2 \left(\frac{h_{z,i,j} - h_{z,i-1,j}}{a_\rho} \right),\end{aligned}\quad (16)$$

where

$$\begin{aligned}\mathcal{F}_{\psi,i,j} &= \frac{1}{\rho_i a_\rho^2} [\rho_{i+1/2} (U_{\rho,i,j} \psi_{i+1,j} - \psi_{i,j}) + \\ &\quad \rho_{i-1/2} (\bar{U}_{\rho,i-1,j} \psi_{i-1,j} - \psi_{i,j})] \\ &\quad + \frac{U_{\theta,i,j} \psi_{i,j+1} - 2\psi_{i,j} + \bar{U}_{\theta,i,j-1} \psi_{i,j-1}}{\rho_i^2 a_\theta^2} \\ &\quad + (1-T) \psi_{i,j} (1 - |\psi_{i,j}|^2).\end{aligned}\quad (17)$$

From the numerical point of view, it is more convenient to evaluate the link variables rather than the vector po-

tential. From equations (12), we can easily verify that

$$\frac{\partial A_{\rho,i,j}}{\partial t} = -\frac{\bar{U}_{\rho,i,j}}{ia_{\rho}} \frac{\partial U_{\rho,i,j}}{\partial t}, \quad \frac{\partial A_{\theta,i,j}}{\partial t} = -\frac{\bar{U}_{\theta,i,j}}{i\rho_i a_{\theta}} \frac{\partial U_{\theta,i,j}}{\partial t}. \quad (18)$$

In addition, from equation (14), we can write, accurate to second order in (a_{ρ}, a_{θ})

$$h_{z,i,j} = \frac{\text{Im}(1 - L_{i,j})}{a_{\rho}\rho_{i+1/2}a_{\theta}}, \quad (19)$$

where $L_{i,j}$ is given by equation (15). Upon introducing equations (18) and (19) into the second and third equations of (16) we obtain the following recurrence relations

$$\frac{\partial U_{\rho,i,j}}{\partial t} = -\frac{i}{\beta} U_{\rho,i,j} \mathcal{F}_{U_{\rho,i,j}}, \quad \frac{\partial U_{\theta,i,j}}{\partial t} = -\frac{i}{\beta} U_{\theta,i,j} \mathcal{F}_{U_{\theta,i,j}}, \quad (20)$$

where

$$\begin{aligned} \mathcal{F}_{U_{\rho,i,j}} &= \text{Im} \left[(1 - T) \bar{\psi}_{i,j} U_{\rho,i,j} \psi_{i+1,j} \right. \\ &\quad \left. + \kappa_{eff}^2 \left(\frac{L_{i,j} - L_{i,j-1}}{\rho_{i+1/2}^2 a_{\theta}^2} \right) \right], \\ \mathcal{F}_{U_{\theta,i,j}} &= \text{Im} \left[(1 - T) \bar{\psi}_{i,j} U_{\theta,i,j} \psi_{i,j+1} \right. \\ &\quad \left. + \kappa_{eff}^2 \frac{\rho_i}{a_{\rho}^2} \left(\frac{L_{i-1,j}}{\rho_{i-1/2}} - \frac{L_{i,j}}{\rho_{i+1/2}} \right) \right]. \end{aligned} \quad (21)$$

Finally, on using the one-step forward-difference Euler scheme with time step Δt , we obtain the following recurrence relations

$$\begin{aligned} \psi_{i,j}(t + \Delta t) &= \psi_{i,j}(t) + \Delta t \mathcal{F}_{\psi_{i,j}}(t), \\ U_{\alpha,i,j}(t + \Delta t) &= U_{\alpha,i,j}(t) \exp \left(-\frac{i}{\beta} \mathcal{F}_{U_{\alpha,i,j}}(t) \Delta t \right), \end{aligned} \quad (22)$$

where $\alpha = (\rho, \theta)$. Notice that equations (22) were written in such a manner they guarantee the link variables are unimodular functions. The first recurrence relation run for all interior vertex points of Ω_{SC} , that is, $\{2 \leq i \leq N_{\rho}, 2 \leq j \leq N_{\theta}\}$; the second ones for all link points in the interior of Ω , that is, $\{1 \leq i \leq N_{\rho}, 2 \leq j \leq N_{\theta}\}$ for $\alpha = \rho$, and $\{2 \leq i \leq N_{\rho}, 1 \leq j \leq N_{\theta}\}$ for $\alpha = \theta$. At the edge points of Ω , the values of the discrete variables will be evaluated using the boundary conditions (see next Section).

There is a severe limitation on the choice of the time step Δt such that the recurrence relations converge. We have learned experimentally that the condition for stability is assured by the following practical rule

$$\Delta t \leq \min \left\{ \frac{\delta^2}{4}, \frac{\delta^2 \beta}{4\kappa^2} \right\}, \quad (23)$$

where

$$\delta^2 = \frac{2}{\frac{1}{a_{\rho}^2} + \frac{1}{r^2 a_{\theta}^2}}. \quad (24)$$

Notice that the stability is controlled by the size of the smallest unit cell. The smaller the value of r , the more severe the restriction on the time step becomes. Perhaps in this case, it would be more convenient to use either a semi or a full implicit scheme to solve equations (20), which are usually unconditionally convergent.

D. The Boundary Conditions

Let \mathbf{n} be a unit vector normal to the $\partial\Omega_{\text{SC}}$ interface and directed outward the domain Ω_{SC} . We will assume that the normal current density vanishes at the superconductor-normal metal interface, that is, $\mathbf{D}\psi \cdot \mathbf{n} = 0$. By using equations (4), it can be shown that the discrete implementation of this condition is as follows

$$\begin{aligned} \psi_{1,j} &= U_{\rho,1,j} \psi_{2,j}, \\ \psi_{N_{\rho}+1,j} &= \bar{U}_{\rho,N_{\rho},j} \psi_{N_{\rho},j}, \\ \psi_{i,1} &= U_{\theta,i,1} \psi_{i,2}, \\ \psi_{i,N_{\theta}+1} &= \bar{U}_{\theta,i,N_{\theta}} \psi_{i,N_{\theta}}. \end{aligned} \quad (25)$$

The first two equations run for all values of $\{2 \leq j \leq N_{\theta}\}$, and the second ones for all values of $\{2 \leq i \leq N_{\rho}\}$. At the corner vertex points of the domain Ω are not necessary to run the recurrence relations (22).

These last four equations update the values of the order parameter at any vertex point at the $\partial\Omega$ interface. The values of the link variables at this interface will be updated by using the fact that the z -component of the magnetic field is continuous at the interface $\partial\Omega_{\text{SC}}$, that is, $h_{z,1,j} = h_{z,N_{\rho},j} = h_{z,i,1} = h_{z,i,N_{\theta}} = H$, which is the external applied magnetic field. Consequently, from equations (14) and (15), the link variables are updated according to

$$L_{i,j} = \exp(-ia_{\rho}\rho_{i+1/2}a_{\theta}H), \quad (26)$$

which runs for all edge points at the interface $\partial\Omega$.

E. The Physical Quantities

The topology of the superconducting state is usually illustrated by $|\psi|^2$. This quantity can be determined from the outcome of the recurrence relations previously derived. Other important physical quantities used to describe the vortex state are the Gibbs free energy, the magnetization, and the vorticity. In what follows we will derive an expression for each of these physical quantities.

- The kinetic energy

$$\begin{aligned}
\mathcal{L}_k &= (1-T) \iint_{\Omega_{\text{SC}}} \left[\left| \frac{\partial(U_\rho \psi)}{\partial \rho} \right|^2 + \left| \frac{1}{\rho^2} \frac{\partial(U_\theta \psi)}{\partial \theta} \right|^2 \right] \rho d\rho d\theta \\
&= (1-T) \sum_{i=2}^{N_\rho} \sum_{j=2}^{N_\theta} \int_{\theta_{j-1/2}}^{\theta_{j+1/2}} \int_{\rho_{i-1/2}}^{\rho_{i+1/2}} \left[\left| \frac{\partial(U_\rho \psi)}{\partial \rho} \right|^2 + \left| \frac{1}{\rho^2} \frac{\partial(U_\theta \psi)}{\partial \theta} \right|^2 \right] \rho d\rho d\theta \\
&= (1-T) \sum_{i=2}^{N_\rho} \sum_{j=2}^{N_\theta} \left\{ \frac{1}{2\rho_i a_\rho^2} \left[\rho_{i+1/2} |U_{\rho,i,j} \psi_{i+1,j} - \psi_{i,j}|^2 + \rho_{i-1/2} |U_{\rho,i-1,j} \psi_{i,j} - \psi_{i-1,j}|^2 \right] \right. \\
&\quad \left. + \frac{1}{2\rho_i^2 a_\theta^2} \left[|U_{\theta,i,j} \psi_{i,j+1} - \psi_{i,j}|^2 + |U_{\theta,i,j-1} \psi_{i,j} - \psi_{i,j-1}|^2 \right] \right\} a_\rho a_\theta \rho_i . \tag{27}
\end{aligned}$$

- The condensation energy

$$\begin{aligned}
\mathcal{L}_c &= (1-T)^2 \iint_{\Omega_{\text{SC}}} |\psi|^2 \left(\frac{1}{2} |\psi|^2 - 1 \right) \rho d\rho d\theta \\
&= (1-T)^2 \sum_{i=2}^{N_\rho} \sum_{j=2}^{N_\theta} \int_{\theta_{j-1/2}}^{\theta_{j+1/2}} \int_{\rho_{i-1/2}}^{\rho_{i+1/2}} |\psi|^2 \times \\
&\quad \left(\frac{1}{2} |\psi|^2 - 1 \right) \rho d\rho d\theta \\
&= (1-T)^2 \sum_{i=2}^{N_\rho} \sum_{j=2}^{N_\theta} |\psi_{i,j}|^2 \left(\frac{1}{2} |\psi_{i,j}|^2 - 1 \right) a_\rho a_\theta \rho_i . \tag{28}
\end{aligned}$$

- The field energy

$$\begin{aligned}
\mathcal{L}_f &= \kappa_{\text{eff}}^2 \iint_{\Omega} h_z^2 \rho d\rho d\theta \\
&= \kappa_{\text{eff}}^2 \sum_{i=1}^{N_\rho} \sum_{j=1}^{N_\theta} \int_{\theta_j}^{\theta_{j+1}} \int_{\rho_i}^{\rho_{i+1}} h_{z,i,j}^2 \rho d\rho d\theta \\
&= \kappa_{\text{eff}}^2 \sum_{i=1}^{N_\rho} \sum_{j=1}^{N_\theta} \frac{[\text{Im}(1 - L_{i,j})]^2}{a_\rho^2 \rho_{i+1/2}^2 a_\theta^2} a_\rho \rho_{i+1/2} a_\theta . \tag{29}
\end{aligned}$$

The total Helmholtz energy is then given by $\mathcal{L} = \mathcal{L}_k + \mathcal{L}_c + \mathcal{L}_f$. The Gibbs free energy can be obtained by a simple modification in the field energy. Instead of h_z^2 we would have $(h_z - H)^2$, or $(h_{z,i,j} - H)^2$ in the discrete version. Notice that the discrete TDGL equations could also be derived through the following equations

$$\begin{aligned}
(1-T) \frac{\partial \psi_{i,j}}{\partial t} &= - \frac{1}{\mathcal{A}_i} \frac{\partial \mathcal{L}}{\partial \bar{\psi}_{i,j}} \\
\beta \frac{\partial A_{\alpha,i,j}}{\partial t} &= - \frac{1}{2\mathcal{A}_{\alpha,i}} \frac{\partial \mathcal{L}}{\partial A_{\alpha,i,j}} , \tag{30}
\end{aligned}$$

where $\mathcal{A}_i = a_\rho \rho_i a_\theta$, $\mathcal{A}_{\rho,i} = a_\rho \rho_{i+1/2} a_\theta$, and $\mathcal{A}_{\theta,i} = a_\rho \rho_i a_\theta$, which are the areas surrounded by the vertex and link points respectively. In order to derive the discrete

TDGL equations by this means, it is essential to use the following relations

$$\frac{\partial U_{\rho,i,j}}{\partial A_{\rho,i,j}} = -i a_\rho U_{\rho,i,j} , \quad \frac{\partial U_{\theta,i,j}}{\partial A_{\theta,i,j}} = -i \rho_i a_\theta U_{\theta,i,j} , \tag{31}$$

which can be easily shown from equations (12).

The magnetization is $4\pi M = B - H$, where B is the magnetic induction which is given by the spatial average of the local magnetic field. We have

$$4\pi M = \frac{1}{\mathcal{A}} \sum_{i=1}^{N_\rho} \sum_{j=1}^{N_\theta} h_{z,i,j} \mathcal{A}_{\rho,i} - H , \tag{32}$$

where \mathcal{A} is total area of the circular sector.

The vorticity can be determined by integrating the phase φ in each unit cell of the mesh. We have,

$$N_{i,j} = \frac{1}{2\pi} \oint_{\mathcal{C}_{i,j}} \nabla \varphi \cdot d\mathbf{r} , \quad N = \sum_{i=1}^{N_\rho} \sum_{j=1}^{N_\theta} N_{i,j} , \tag{33}$$

where $\mathcal{C}_{i,j}$ is a closed path with lower left and upper right corner at (i, j) and $(i+1, j+1)$, respectively.

In all of our numerical simulations described in the next Section, we calculated N in order to make sure that the number of vortices agrees with what we see on the topological map of the order parameter.

IV. RESULTS AND DISCUSSION

The recurrence relations derived in the previous Section were implemented as follows. We started from the Meissner state, where $\psi = 1$ and $U_\rho = U_\theta = 1$ everywhere as the initial condition. Then we let the time evolves until the system achieves the stationary state.¹⁴ This is done by keeping the external applied magnetic field H constant. Next, we ramp up the applied field by an amount of ΔH . The stationary solution for H is then used as the initial state to determine the solution for $H + \Delta H$, and so on. Usually we started from zero field and increased

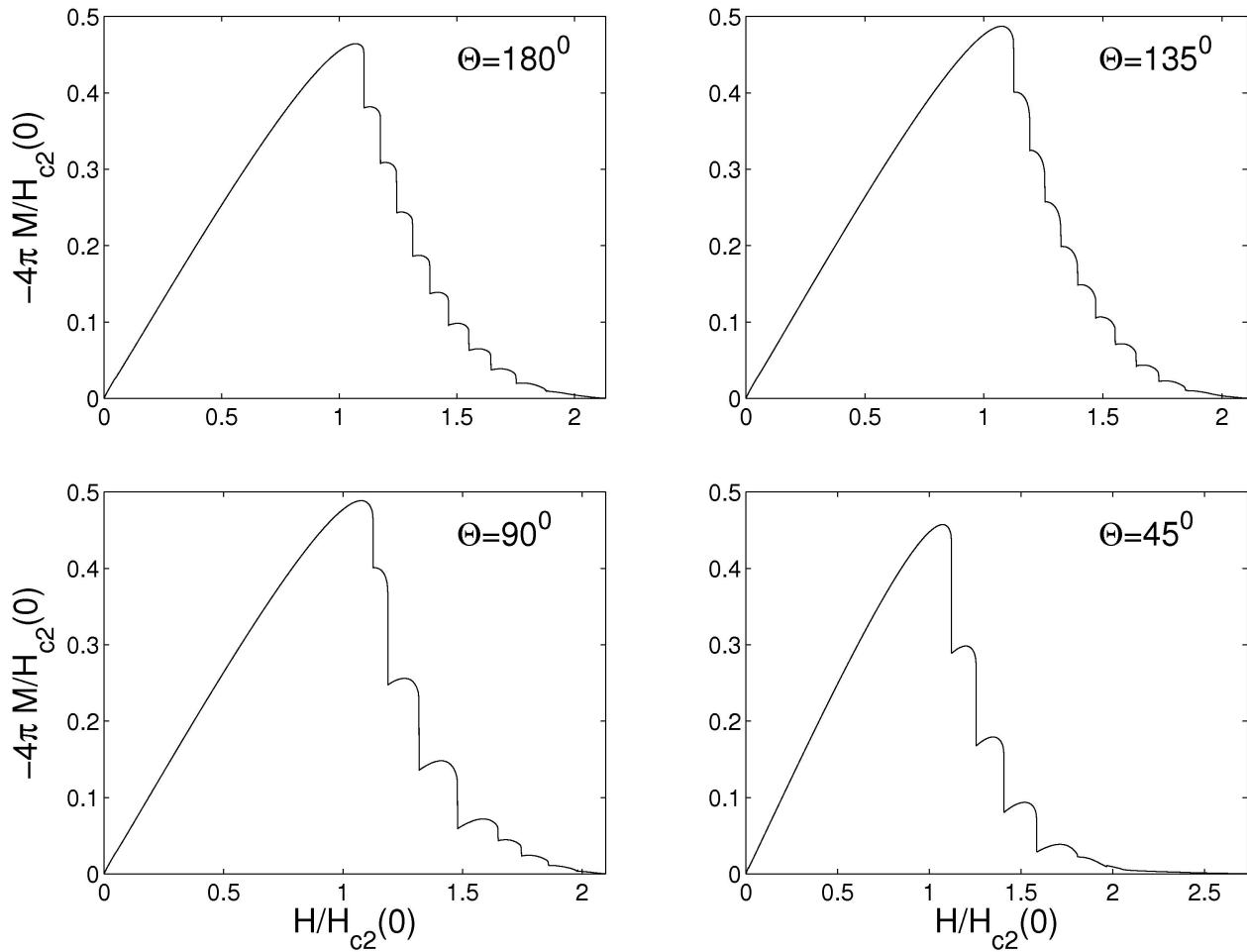


FIG. 2: The magnetization curve as a function of the external applied magnetic field for four values of the angular width of the circular sector. Each jump in the magnetization indicates a phase transition. The corresponding configuration for each phase is indicated in Table I.

H until superconductivity is destroyed. As a criterion for termination of the simulation, we monitored the Gibbs free energy as a function of H . When the value of this quantity changes its sign, then the transition from the superconducting to the normal state sets in.

The parameters used in our numerical simulations were $\kappa = 0.28$, which is a typical value for Al;² the other parameters are $d = 0.1$, $T = 0$, and $\beta = 1$. The internal radius and the area of the circular sector were taken fixed for any value of angular width Θ . We used $r = 1/\pi$ and 16π for the area, such that the external radius is given by $R = \sqrt{32\pi/\Theta + r^2}$. The reason for taking these parameters as such is because it makes possible comparison between our results and previous ones (see Ref. 8, and References therein). The size of the mesh varied according to the value of Θ . As a criterion we have taken the length of the most external unit cell no larger than 0.25×0.25 . Since the order parameter varied most significantly over a distance $\xi(T)$ (in real units), we are certain of not losing this variation within this criterion. We

ramp up the applied magnetic field, typically in steps of $\Delta H = 10^{-3}$.

In Fig. 2 we present the magnetization versus external applied magnetic field curves for several values of the angular width. These pictures present a typical profile of a magnetization curve of a mesoscopic superconductor. It presents a series of discontinuities, in which each jump signals the entrance of more vortices into the sample. Notice that the lower critical field does not vary with the shape of the circular sector. From this, the immediate conclusion is that it depends only on the area but not on Θ . This is not an obvious result. In fact, in Ref. 8 numerical simulations were performed in three different geometries: disk, square, and triangle and using the same parameters as in the present contribution. They find that the magnitude of the lower critical field is the same for the disk and the square, but slightly larger for the triangle, despite all geometries having the same area. Since we have the freedom to deform the circular sector, it should be expected similar behavior for the lower critical field,

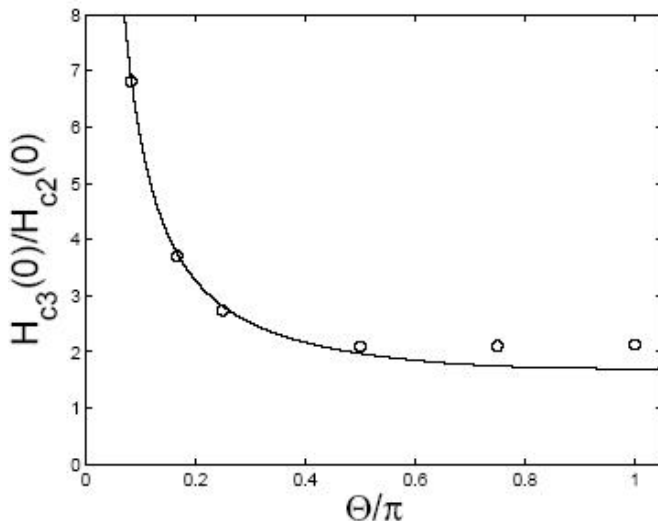


FIG. 3: The nucleation field as function of the angular width of the circular sector. The solid line corresponds to equation (34) taken from Ref. 3 and the open circles are the results found in the present simulation.

especially for small width angles Θ . However, the results shown in Fig. 2 do not seem to exhibit this feature.

Another interesting feature present in the pictures of Fig. 2 is that the SN transition field $H_{c3}(T)$ is approximately the same for all angles greater than 90° . In addition, $H_{c3}(T)$ is approximately the same for a disk and a square of equivalent area. However, for smaller values of Θ , this critical field becomes significantly larger. Indeed, in Ref. 3 $H_{c3}(T)$ was calculated numerically for a wedge. The area they used for the wedge is 2.33 larger than the one we used here. They found that their results fit quite well into the following expression

$$\frac{H_{c3}(T)}{H_{c2}(T)} = \frac{\sqrt{3}}{\Theta} \left(1 + 0.14804\Theta^2 \frac{0.746\Theta^2}{\Theta^2 + 1.8794} \right). \quad (34)$$

In Fig. 3 we depict both the above expression and what we have found for the nucleation field $H_{c3}(0)$ as a function of Θ/π . As can be seen from that Figure, for large angles, the nucleation field is larger in the geometry we consider. This suggests that, had we diminished the area of the circular sector, this difference for large angles would have increased. Nonetheless, for small angles all curves should collapse into a single curve, which corresponds to the asymptotic behavior $H_{c3}(T)/H_{c2}(T) = \sqrt{3}/\Theta$ determined in Ref. 3. This suggests that the superconductor behaves as an unidimensional system as Θ becomes small, no matter what the area is.

We also investigated the topology of the order parameter. Before going any further, let us establish the criterion we use to distinguish a single vortex from a giant vortex state. A giant vortex is nucleated as two or more vortices collapse into a single vortex in which all of them have, rigorously, a common core center. To describe an N vortex state we use the following nomenclature. We

TABLE I: The sequence of vortex configurations for four different angles of the circular sector. The nomenclature used is explained in the text. The configurations in brackets corresponds to what we obtain not using a logarithm scale.

N	180°	135°	90°	45°
1	1S	1S	1S	-
2	2S	2S	-	2S
3	3S	3S	3S	-
4	4S	4S	-	4S
5	5S	5S	5S	-
6	6S	6S	-	6S
7	7S	7S	7S(5S1G ₂)	-
8	8S	8S(6S1G ₂)	8S(5S1G ₃)	8S(5S1G ₃)
9	9S	9S(4S1G ₅)	9S(5S1G ₄)	9S(4S1G ₅)
10	10S(4S1G ₆)	10S(4S1G ₆)	10S(3S1G ₇)	10S(5S1G ₅)
11	11S(5S1G ₆)	11S(2S1G ₉)	11S(3S1G ₈)	11S(4S1G ₇)

denote by $N_s S$, a multiple vortex configuration formed by N_s single vortices. A single giant vortex of vorticity N_g is denoted by $1G_{N_g}$. For example, the $4S1G_2$ state is formed by four single vortices and a double quantized giant vortex.

In all geometries we have considered, usually it occurs transitions either from N to $N + 1$ or from N to $N + 2$ vortices. In Fig. 4 and 5 we depict $|\psi|$ for $\Theta = 180^\circ$ and $\Theta = 45^\circ$ respectively, and two stationary states with different values of H . We have chosen transitions where we could have the formation of a giant vortex. As can be seen in these figures, we have the transitions $9S \rightarrow 4S1G_6$ ($\Theta = 180^\circ$) and $6S \rightarrow 5S1G_3$ ($\Theta = 45^\circ$).¹⁵ However, if we look at the same pictures in a logarithm scale, we still see that the core centers of the vortices occupy different positions. So, within this criterion, we cannot affirm that a giant vortex has been nucleated. For higher vorticity, we have not observed any giant vortex either. A very different scenario takes place in disks, squares, and triangles even using the same parameters as in the present work.⁸ Maybe, for smaller areas, giant vortex could be formed; we have not tested this possibility. All possible configurations are summarized in Table I up to $N = 11$. Notice that the vortices are always symmetrically distributed along the mediatrix.

V. SUMMARY

In summary, an algorithm has been developed for solving the Ginzburg-Landau theory for circular geometries. This will probably make much easier to extend the ψU method for other geometries in addition to the circular and rectangular ones. Furthermore, we have applied the algorithm to circular sector and have found several configurations for the vortex state in this geometry. Also, the superconducting nucleation field has been evaluated. We

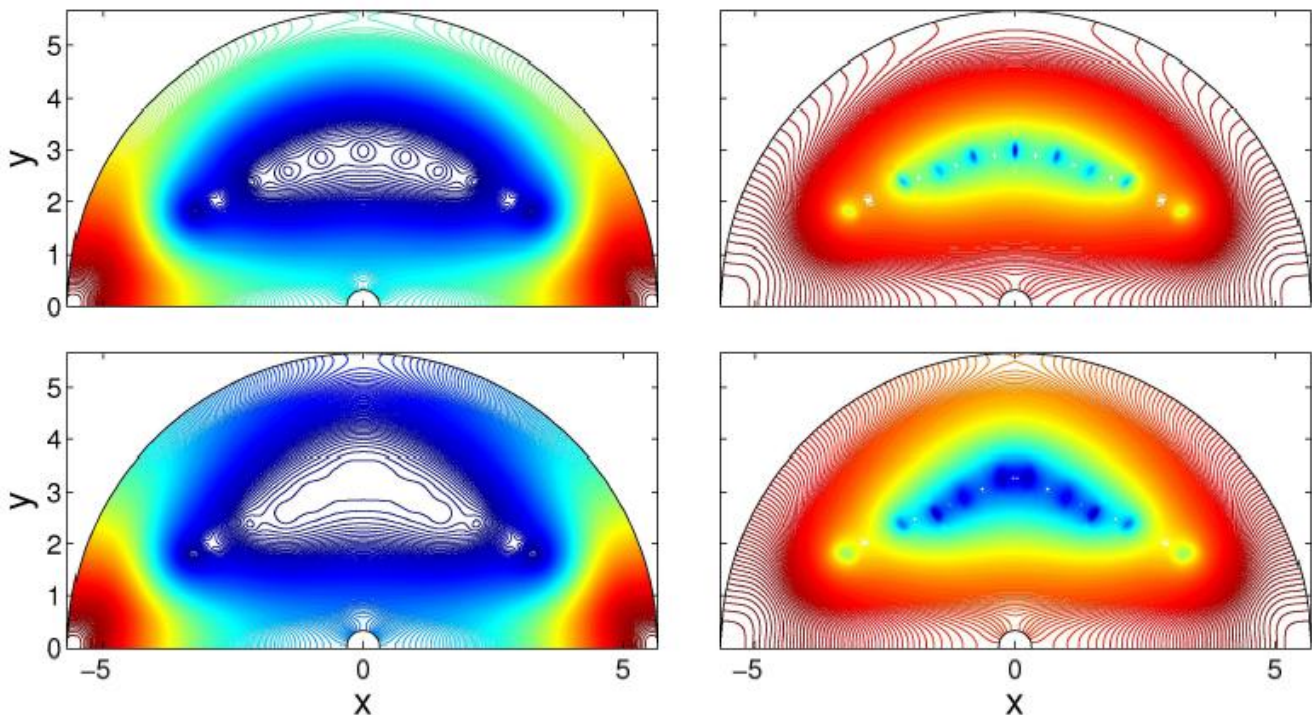


FIG. 4: (Color online) Two dimensional density contour plots of $|\psi|$ for an angular width of $\Theta = 180^\circ$ with $N = 9$ and $N = 10$ vortices, from the top to the bottom (left column; the right column corresponds to the same pictures, but in logarithm scale). Both pictures correspond to the stationary states as the vortices enter the sample. Notice that, once the equilibrium configuration is achieved, the vortices are symmetric with respect to the vertical axis. This feature is always present in the other geometries.

have presented some evidences that, as we diminishes the area of the superconductor, the nucleation field increases. However, as the angular width goes to low values, this field exhibits an universal behavior, independently of the area.

Acknowledgments

The authors thank the Brazilian Agencies FAPESP and CNPq for financial support, and Dr. and Clecio C.

de Souza Silva for useful discussions.

-
- ¹ G. R. Berdiyrov, B. J. Baelus, M. V. Milošević, and F. M. Peeters PRB **68**, 174521 (2003).
² V. V. Moshchalkov *et al.* in *Connectivity and Superconductivity*, edit by J. Berger and J. Rubinstein (Springer, Heidelberg, 2000).
³ V. A. Schweigert and F. M. Peeters, Phys. Rev. B **60**, 3084 (1999).
⁴ A. Kanda, B. J. Baelus, F. M. Peeters, K. Kadowaki, and Y. Ootuka, PRL **93**, 257002 (2004).
⁵ T. Nishiro, S. Okayasu, J. Suzuki, and K. Kadowaki, Physica C **412-414**, 379 (2004).
⁶ S. Okayasu, T. Nishio, Y. Hata, J. Suzuki, I. Kakeya, K. Kadowaki, and V. V. Moshchalkov, IEEE Trans. Appl. Supcond. , 678 (2005).
⁷ E. Sardella, A. L. Malvezzi, P. N. Lisboa-Filho, and W. A. Ortiz, Phys. Rev. B **75**, 014512 (2006).
⁸ B. J. Baelus and F. M. Peeters, Phys. Rev. B **65**, 104515 (2002).
⁹ A. Schmid Phys. Kondens. Materie **5**, 302 (1966).
¹⁰ W. D. Gropp, H. G. Kaper, G. K. Leaf, D. M. Levine, M. Palumbo, and V. M. Vinokur, J. Comput. Phys. **123**, 254 (1996).
¹¹ G. C. Buscaglia, C. Bolech and A. López, *Connectivity and Superconductivity*, J. Berger, and J. Rubinstein (Eds.), Springer, 2000.
¹² J. Pearl, Appl. Phys. Lett. **5**, 65 (1964).

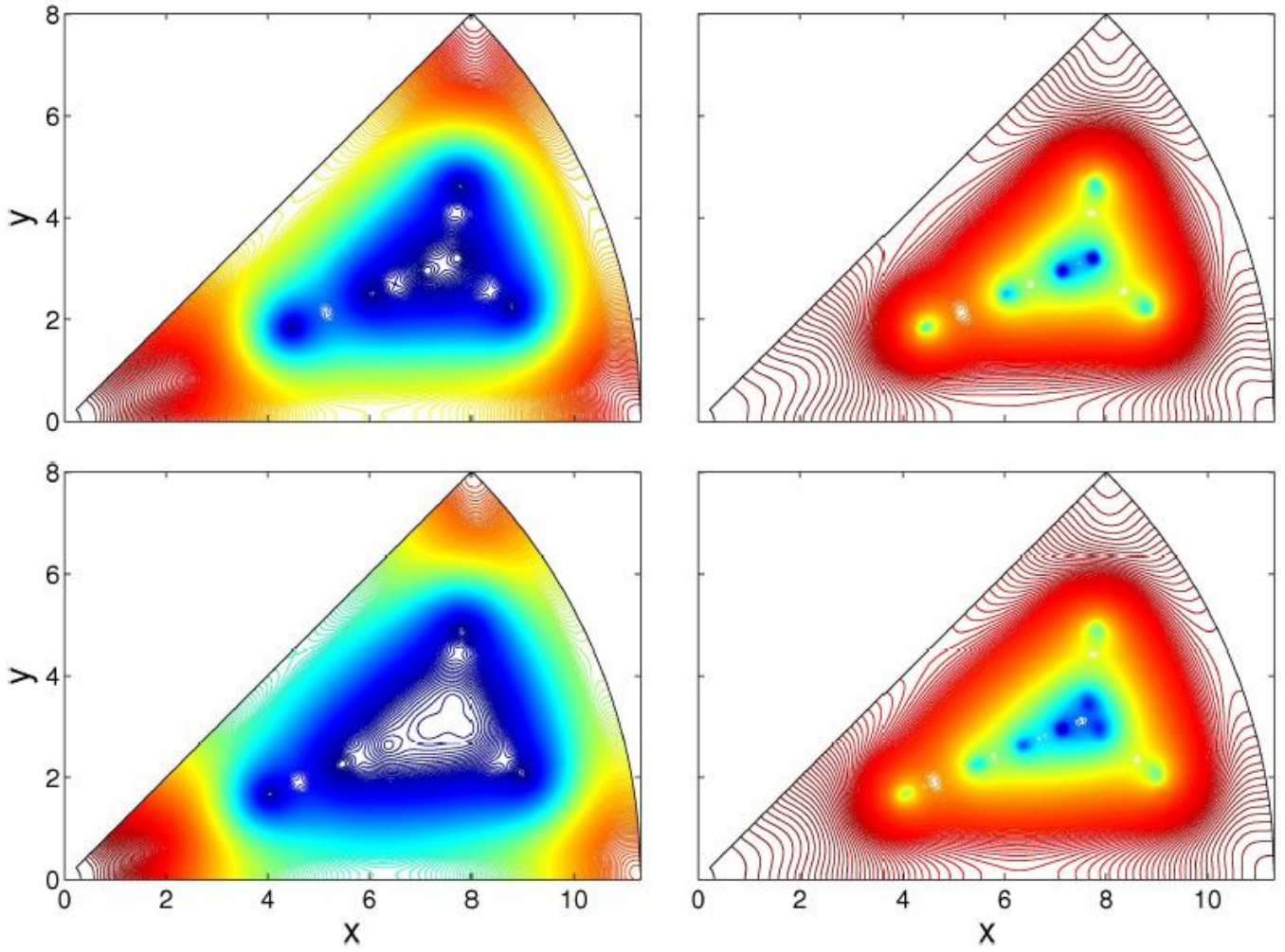


FIG. 5: (Color online) The same as Fig. 4 for $\Theta = 45^\circ$ with $N = 6$ and $N = 8$.

¹³ G. R. Berdiyrov, M. V. Milosevic, and F. M. Peeters, *Physica C* **437-438**, 25 (2006).

¹⁴ We use the following criterion for the stationary state: if the highest difference $||\psi(t) - |\psi(t + \Delta t)||$, for any vertex point in the mesh, is smaller than a certain precision ϵ , then we go over the next field. We have worked with a precision of $\epsilon = 10^{-6}$ for $\Theta = 45^\circ$ and $\epsilon = 10^{-5}$ for the

other angular widths.

¹⁵ We have used the highest resolution as possible in order to detect an individuality in the vortex configurations. Beyond some critical resolution, the pictures do not present an change.